Statistical Analysis of Magnetopause Response During Substorm Phases

Sanjay Kumar [1] and Tuija I. Pulkkinen [1]

[1]Department of Climate and Space Sciences and Engineering, University of Michigan, Ann Arbor, MI, USA

Correspondence: Sanjay Kumar (kumarsa@umich.edu)

Abstract. We investigate variations in the position of the magnetopause in response to the interplanetary magnetic field (IMF), and different phases of magnetospheric substorms. The average location of magnetopause is examined using magnetic field observations from multiple satellites (THEMIS, RBSP, and MMS), and the Shue model utilizing OMNI solar wind data for a period of five years from 2016-2020. We estimate average position of the magnetopause using Shue model through superposed epoch analysis of standoff distance and tail flaring angle at different substorm timings (onset, peak and end) and from in-situ measurements through 2D equatorial maps of average B_Z under IMF $|B_Z| > 0$ conditions. We found that southward IMF is associated with a greater number of substorms compared to northward IMF orientations. Our analysis highlights a very small movement of the magnetopause during substorm phases for both northward and southward IMF orientations ($|B_Z| > 0$). Notably, magnetopause experiences an inward movement, reaching its closest point to the Earth, particularly during the substorm growth phase followed by a relaxation from substorm peak to recovery end. The empirical model provides accurate estimation of the magnetopause location during periods of both northward and southward IMF $|B_Z| > 0$, as the model curve traverses a distinct location representing the magnetopause shown in the 2D average map of observed B_Z.

1 Introduction

The magnetopause is the boundary of the Earth's magnetosphere which separates the magnetic cavity from the surrounding plasma environment. The location of the magnetopause is determined by the pressure balance between magnetospheric magnetic field and the solar wind. The magnetopause is not stationary, being strongly influenced by the solar wind dynamic pressure (Chapman and Ferraro, 1931), the interplanetary magnetic field (IMF) orientation and strength (Fairfield, 1971; Shue et al., 1997, 1998), and dipole tilt angle (Liu et al., 2012). The solar wind pressure changes move the magnetopause, sometimes to inside geosynchronous orbit ($\sim 6.6\ R_E$, R_E = Earth radius) (Cahill and Winckler, 1999). Furthermore, strongly southward IMF leads to inward motion of the magnetopause due to magnetic flux erosion from the dayside magnetopause via magnetic reconnection and during periods of sharp increases in solar wind dynamic pressure (Tsyganenko and Sibeck, 1994). Although, reconnection only causes minimal inward motion as the thickness of subsolar magnetopause is typically only a few hundred kilometers thick (Paschmann et al., 2018).

Several models parameterize the magnetopause location and shape by solar wind and IMF parameters (Chao et al., 2002; Fairfield, 1971; Sibeck et al., 1991; Lin et al., 2010; Liu et al., 2015; Nguyen et al., 2022, and references therein). Shue et al.

(2000) reviewed many magnetopause models and compared the differences among them for extreme solar wind conditions and their limitations. Shue et al. (1997) studied the magnetopause location using in-situ magnetopause crossings by multiple satellites to construct an empirical model that incorporates the influence of solar wind dynamic pressure and IMF B_Z on controlling the location and shape of the magnetopause.

Wang et al. (2018) studied the effects of IMF north-south orientation and upstream solar wind dynamic pressure on the location of the magnetopause and bow shock using a global MHD model. They found that during southward IMF and high solar wind pressure, increased reconnection moves the magnetopause earthward and outward for positive IMF B_Z. They also conclude that the effect of dynamic pressure on magnetopause location is more prominent than those due to the IMF orientation changes. Lu et al. (2011) constructed a magnetopause model through global MHD calculations and observed that IMF B_Z primarily influences the magnetopause shape with minor effects on standoff distance. In contrast, solar wind dynamic pressure predominantly affects the magnetopause standoff distance with minimal impact on the magnetopause shape.

Substorms are dynamic and transient phenomena that play a crucial role in the Earth's magnetosphere, storing solar wind energy and then releasing it through an explosive process(Baker et al., 1996). Substorms represent a key dynamic cycle in the solar wind – magnetosphere – ionosphere system, with the coupling involving intensification of auroral currents (Akasofu, 1964). Several studies have proposed that substorms are triggered by changes in the solar wind driver: While substorm onsets are often followed by an interval of southward IMF (Kokubun, 1972), northward turnings of the IMF can also be responsible for triggering substorms (Mcpherron et al., 1986; Sergeev et al., 1986). While Wild et al. (2009) concluded that substorm onsets occur following an IMF southward turning and at least 20-min interval of southward IMF. Furthermore, Hsu (2003) considered changes in IMF B_Y, dynamic pressure, and IMF B_Z changes and concluded that majority of the substorms are triggered by IMF B_Z change, while a rather small number are triggered by IMF B_Y rotation or change of dynamic pressure, while some substorms have no identifiable external trigger (Henderson et al., 1996). Aubry et al. (1970) observed inward motion of magnetopause and its relation to an increase in the tail flux and substorm onset using satellite observations. They found earthward motion of magnetopause during reversal of IMF B_Z from northward to southward just prior to substorm onset which continues for two hours with the magnetopause moving inward up to 2 R_E.

In this paper we present statistical investigation of average location of magnetopause for northward-southward IMF during different phases of substorms. Focusing on a period of 5 years from 2016-2020, we use satellite observations from Radiation Belt Storm Probes (RBSP) (Mauk et al., 2013), Time History of Events and Macroscale Interactions during Substorms (THEMIS) (Angelopoulos, 2008), and Magnetospheric Multiscale (MMS) (Burch et al., 2016), which provide a very good coverage of magnetosphere out to 30 R_E in the dayside. We complement the space measurements with data from ground-based magnetometers available from the SuperMAG collaboration (Gjerloev, 2012). For this study period we identified 5077 isolated substorms from a list of substorm onsets created by Ohtani and Gjerloev (2020). We use superposed epoch analysis to estimate the average standoff distance and tail flaring angle taken from the nonlinear relation given by Shue et al. (1998) in their empirical model for magnetospheric shape and size. We also discuss the application of Shue model in the estimation of average magnetopause location observed in this study. Section 2 describes the data, Section 3 presents average map of observed

60 magnetic field in the equatorial plane during substorms phases and Section 4 presents a superposed epoch analysis, 5 shows the empirical model by Shue and Section 6 concludes with discussion of results.

2 Data

We examine the magnetospheric signatures of substorms during the interval of 2016–2020, when several (multisatellite) missions were operational. We use data from the three Time History of Events and Macroscale Structures during Substorms
65 (THEMIS) in near-Earth near-equatorial orbits (Apogee $\sim 12 R_E$), from the two Radiation Belt Storm Probes (RBSP) in the inner magnetosphere inside of about $\sim 6 R_E$, and from one of the Magnetospheric Multiscale (MMS) spacecraft in near-equatorial, higher-altitude orbit (Apogee $\sim 25 R_E$). Although the MMS mission involves four spacecraft, their close formation is such that incorporating observations from more than one spacecraft is not pertinent to this study. The orbits of the RBSP, THEMIS and MMS satellites are near the equatorial plane, which corresponds to low latitudes. These missions are designed
70 to investigate key processes in the magnetosphere, many of which occur in the near-equatorial plane.

We use magnetic field data from the EMFISIS instrument suite (Kletzing et al., 2013) onboard both RBSP-A and RBSP-B spacecraft. We also use spin-averaged magnetic field data from the Fluxgate Magnetometer (FGM) (Auster et al., 2008) from THEMIS-A,D, and E (Excluding THEMIS-B and THEMIS-C, which orbit around the Moon). Magnetic field data from the MMS-1 spacecraft come from the Fluxgate magnetometer (Russell et al., 2016). All observations (magnetic field and spacecraft
75 position) used in this study are averaged over 1-minute intervals and examined in the geocentric solar magnetospheric (GSM) coordinates.

We use time series of SuperMAG Auroral Electrojet (SML) index, solar wind and interplanetary magnetic field (IMF) data at 1-min time resolution from the SuperMAG database (https://supermag.jhuapl.edu/indices/, Gjerloev (2012)). The solar wind data on the SuperMAG site come from the OMNI database (https://omniweb.gsfc.nasa.gov/). The list of isolated substorm
80 onsets comes from Ohtani and Gjerloev (2020), who identified substorm onsets using the SML index. During the period from 2016 to 2020, there were 5,077 substorms identified, and we found the substorm peak times (corresponding to the minimum SML) and end times (when SML recovers to above -100 nT) (see Kumar et al. (2024) for details).

In order to assess the magnetopause location as function of the solar wind parameters, we use formulation introduced by Shue et al. (1998) that gives the position and shape of the magnetopause in the form:

$$r = r_0 \left[\frac{2}{1+\cos\theta} \right]^{\alpha} \tag{1}$$

$$r_0 = [10.22 + 1.29 \tanh(0.184(B_Z + 8.14))] P^{-1/6.6} \tag{2}$$

$$\alpha = (0.58 - 0.007 B_Z)[1 + 0.24 \ln(P)], \tag{3}$$

where r is the radial distance from the Earth and θ is the solar zenith angle computed from the positive X_{GSM}-axis. The parameter r_0 gives the standoff distance at the subsolar point, and α determines the level of tail flaring.

3 Magnetopause observations

We examine the external magnetic field using combined datasets from spacecraft (THEMIS-A,D, E, RBSP-A, B, and MMS-1) during different phases of substorms and for five years 2016–2020. In Figure 1(a-f), the observed magnetic field B_Z is represented through color-coded maps. These maps are created by averaging the magnetic field values in $1R_E \times 1R_E$ bins of X and Y. The maps provide visual representations of the variations in field strength within the dayside regions of the Earth. The maps utilize 5 minutes data of B_Z collected prior to onset (Pre-onset), after the substorm peak (Post-peak), and before the substorm end (Pre-end) for northward IMF (a, c, e) and southward IMF (b, d, f). In Figure 1, the average B_Z is presented in the X-Y (equatorial) plane of magnetosphere during substorm growth (Pre-onset), early recovery (Post-peak) and late recovery (Pre-end) phases for northward IMF (IMF $\langle B_Z \rangle > 0$ nT, a, c, e) and southward IMF (IMF $\langle B_Z \rangle < 0$ nT, b, d, f) separately. The near-equatorial orbits of the spacecraft result in the most comprehensive data coverage being in the equatorial region (see Figure 2 in Kumar et al. (2024)). First, we aggregate magnetic field measurements from all satellites over the five-year period, resulting in nearly 15 million data points when averaged over 1-minute intervals. This magnetic field data is combined with solar wind data, specifically the IMF B_Z and dynamic pressure, obtained from the OMNI database and also averaged over 1 minute. We utilize a predefined list of substorms and develop an algorithm to identify the time intervals from the onset to the end of each substorm. This approach enables us to compute the average of IMF B_Z for each substorm period (from onset to recovery end), offering insight into the typical value of IMF B_Z during each event. We then filter the data based on IMF B_Z values, distinguishing between IMF $B_Z > 0$ (northward IMF) and IMF $B_Z < 0$ (southward IMF). This allows us to estimate the number of substorms occurring under both northward and southward IMF conditions. During the study period from January 1, 2016, to December 31, 2020, we observed a total of 5,077 isolated substorms. Of these, the majority of substorms (3,458) occurred during periods of southward IMF, compared to 1,502 substorms during northward IMF. Additionally, 117 substorms occurred independently of any IMF changes. The reason for choosing substorms during northward/southward IMF is that there is a strong correlation between IMF B_Z and the occurrence of magnetospheric substorms. The more prolonged and intense southward IMF B_Z, the more energy is transferred into the magnetosphere, leading to more frequent and intense substorms. When the IMF B_Z is northward, the probability of substorm occurrence is lower. However, substorms can still occur, often due to other processes or prior build-up of energy in the magnetotail. In Figure 1, we illustrate the Earth at the center with a radius of 1 R_E. The region within 4 R_E around the Earth is masked, as we focus on the region outside that distance, and the black circle at 6.6 R_E provides a reference to geostationary orbit. Each panel in Figures 1 and 2 consists of 861 bins, but the number of data points per bin varies. In the panels showing in Figures 1a, 1c, 1e, for northward IMF, the number of data points ranges from 0 (lighter bins) to a maximum of 351 (darker bins). In contrast, the panels depicting in Figures 1b, 1d, 1f for southward IMF contain more data points, with counts ranging from 0 to a maximum of 700, reflecting the higher number of substorms during southward IMF periods.

In Figure 1 (a, c, e), the black curves are plotted on the average magnetic field B_Z maps using the standoff distance r_0 and tail flaring angle α obtained from the empirical model by Shue et al. (1998). To plot these black curves, we initially utilize equations (2) and (3) for r_0 and α, respectively. We then estimate their average values near all the 5077 substorm onset, peak,

and end times from Figure 3 (j-o) for strong northward IMF, where strong northward IMF is defined as IMF $B_Z > 5$. Using average values of r_0 and α around all onset, peak, and end times of substorms, we estimate radial distance r from equation (1) and finally calculate the positions x_s and r_s using $x_s = r * cos(\theta)$, $r_s = r * sin(\theta)$. In Figure 1 (a, c, e), the black curves representing x_s versus r_s do pass through the high magnetic field regions (green color) within the magnetopause. However, it is important to note that these curves may not accurately represent the average location of the magnetopause. The red dashed curves in Figure 1 (a, c, e) are plotted exactly in the same manner as black curves but for northward IMF, which is defined as IMF $B_Z > 0$. For these curves, we first estimate r_0 and α from figure similar to Figure 3 (j-o) (not shown) but for northward IMF. The red curves in Figure 1 (a, c, e) pass very close to the thin boundary between yellow and green color, indicating a relatively accurate representation of the average magnetopause location.

Figures 1 (b, d, f) are plotted in the same way as Figures 1 (a, c, e) representing a color-coded map of averaged magnetic field B_Z from growth to recovery end phases of substorm but for southward IMF (IMF $B_Z < 0$). In the Figures 1(b, d, f), the magnetopause is clearly identified between yellow and green colours. The red dashed curves plotted (same as in Figure 1 a, c, e) using Shue et al. (1998) model over the averaged magnetic field B_Z maps for northward IMF (IMF $B_Z > 0$) pass through the boundary between the yellow and green colours also confirm (as in the Figure 1 (a, c, e)) the location of outer boundary of magnetosphere. Similar to Figure 1 (a, c, e), the plotting of black curves (for strong southward IMF (IMF $B_Z < -5$)) follows the same methodology.

Figure 2 shows difference maps indicating the time evolution of dayside B_Z averaged for $1 R_E \times 1 R_E$ bins in X and Y during substorm onset to peak (Pre-peak – Pre-onset), around the substorm peak (Post-peak – Pre-peak), and from the substorm peak to end of the recovery phase (Pre-end – Post-peak) during northward IMF ($\langle B_Z \rangle > 0$) (a, c, e) and southward IMF ($\langle B_Z \rangle < 0$) (b, d, f). Each panel shows color-coded 2D difference map of a 5-min average data of B_Z with positive values (indicating an increase in the magnetic field) displayed in red, and negative values (indicating a decrease in the magnetic field) shown in blue colors. The curves (black, cyan dashed) are identical to those in Figure 1. These curves in the left panels (Figure 2 a, c, e) represent cases with northward IMF, specifically with IMF $B_Z > 5$ nT (0 nT), while the right panels (Figure 2 b, d, f) depict cases with southward IMF, corresponding to IMF $B_Z < -5$ nT (0 nT).

The difference maps for the expansion phase (Figures 2a, b) demonstrate that during this phase (Pre-peak - Pre-onset), the magnetic field outside the magnetopause in the magnetosheath increases (shown by red colors), more prominently in both the northward IMF and southward IMF case. As the magnetosheath field is created by the shocked IMF, this is an indication of an IMF maximum at the substorm onset time.

The field inside the dayside magnetosphere shows more complex behavior. For northward IMF (Figure 2 a), between the magnetopause and geostationary orbit, the dayside field change is predominantly negative, but inside geostationary orbit the field change is mildly positive. This would be consistent with an enhancement of the ring current in that sector, with field enhancement inside the current peak and field reduction outside of it.

We also point out that there is a bipolar structure with field increase inside geostationary orbit and field decrease outside of it in the morning sector (Figure 2 a), and the opposite changes in the evening sector near the terminator.
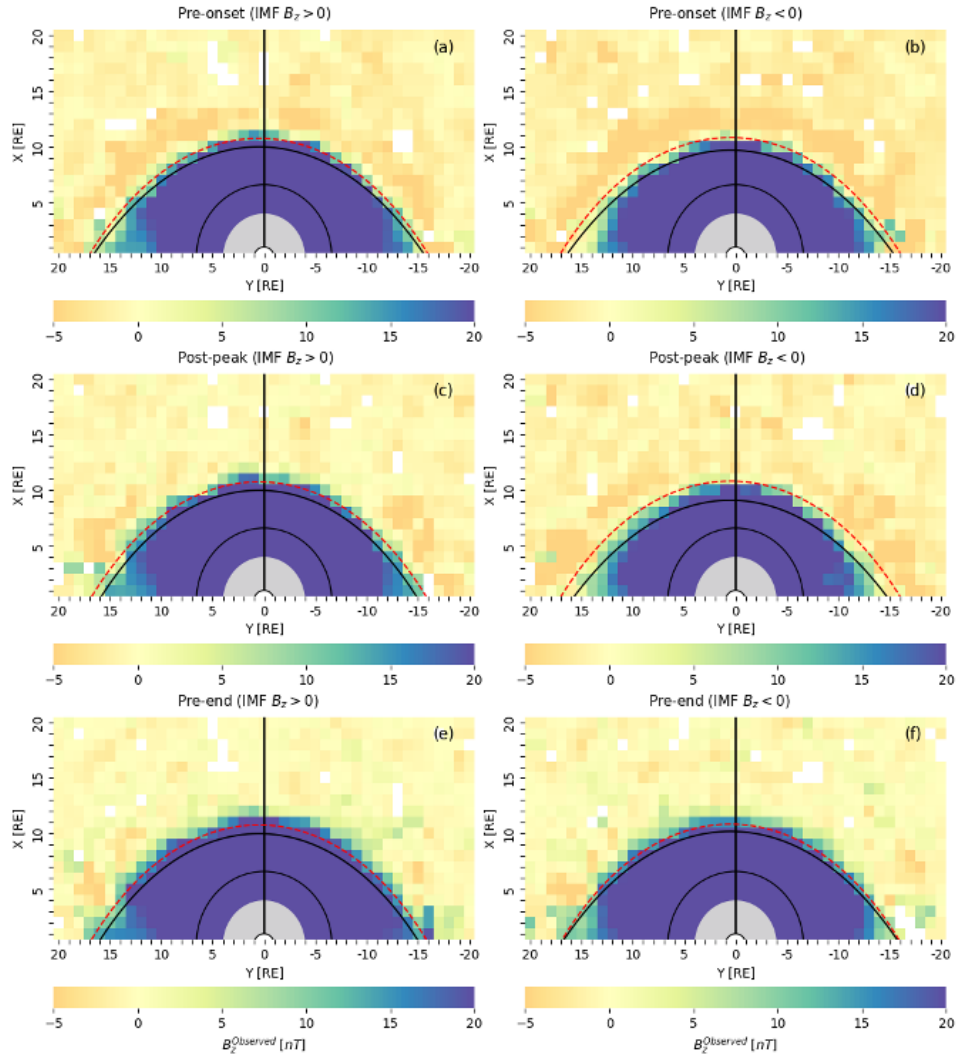
Figure 1. Average magnetic field B_Z in the equatorial plane averaged over 5 min before the substorm onset (pre-onset, a, b), 5 min after the peak (post-peak, c, d), and 5 min before the end (pre-end, e, f) for northward IMF ($\langle B_Z \rangle > 0$ nT, a, c, e) and southward IMF ($\langle B_Z \rangle > 0$ nT, b, d, f) are shown separately. The black (red dashed) curves are plotted using Shue et al. (1998) model with IMF $B_Z > 5$ (0) nT for northward IMF (left panels) and with IMF $B_Z < -5$ (0) nT for southward IMF (right panels).

For the southward IMF case (Figure 2 b), the dayside field is strongly negative under black (dashed cyan) curve, could be implying a strong ring current enhancement. As the field depression is negative throughout the region, the ring current peak is likely closer to the Earth, as particles under southward IMF and stronger convection have access to closer drift paths around the Earth. The bipolar structure is not visible for the southward IMF case.

As the substorm reaches its peak and the recovery starts, the positive field change outlines the magnetopause, indicating an outward motion of the magnetopause Figures 2 (c, d). Other changes inside the magnetosphere are mostly small. The substorm recovery phase (Figures 2 e, f) causes a strong signal around the magnetopause for both northward and southward IMF cases, implying further outward motion (relaxation) of the magnetopause.

For both cases, the dawn and dusk fields are strongly enhancing from inside geostationary orbit out to the magnetopause.

The field continues to increase around the substorm peak time, with mostly red colors indicating further relaxation. Moreover, the field continues to increase strongly beyond the substorm peak, as demonstrated by strongly positive (dark red) values during the late recovery phase as shown by in-situ measurements (Figure 2 e, f). However, the Shue magnetopause exhibits a relaxation of the magnetic field (moving outward) from post-peak to pre-end, with its position changing from 10.28 to 10.29 R_E (Table 1). Although, the outward movement of magnetopause is very small shown in in-situ measurements but same tendency of outward movement during substorm recovery phase is supported by the Shue model as well.

Figure 2 b depicts that from Pre-onset to Pre-peak, the dayside magnetic field is not in a relaxing state and experiences a decrease, as indicated by mostly blue colors and the magnetopause exhibits antisunward motion or compression.

This behavior is the same as shown by the Shue magnetopause, which shows a compression (albeit very small) of the magnetopause from Pre-onset to Pre-Peak, with its position changing from 10.27 to 10.26 R_E (Table 1). Around the substorm peak (from Pre-peak to Post-peak), the field increases, indicated by mostly red colors, signifying slight sunward motion of magnetopause. This pattern aligns with the empirical model results illustrated in Figures 1 c. The field continues to increase strongly from the substorm peak to the recovery end, as indicated by strongly positive (dark red) values of the magnetic field during the recovery end (Figure 2 e, f). Similar to the case of a northward IMF, the Shue magnetopause exhibits a relaxation of the magnetic field from post-peak to pre-end, with its position changing from 10.33 to 10.37 R_E (Table 1).

The difference maps (Figures 2 b, d, f) show that during the Pre-Peak - Pre-Onset phase, the dayside magnetospheric field is reduced (predominantly blue colors), indicating inward motion of the magnetopause. The changes around the substorm peak time are predominantly positive, indicating further expansion of the field (consistent with the empirical model results), and even more strongly positive during the recovery phase.

4 Superposed Epoch Analysis

Superposed epoch analysis is a statistical technique used to identify patterns in time series associated with specific events. The method allows examination of average system response centered around the zero epoch. We use three zero epoch as substorm onset (SML onset), substorm peak (SML minimum), and substorm end (SML recovery to above -100 nT).

Figure 3 displays the superposed epoch analysis for strongly northward IMF defined as $\langle B_Z \rangle > 5$ nT during the epoch period from substorm onset to recovery end. The panels show the observed SML index, IMF B_Z, solar wind dynamic pressure P_{dyn}, and the magnetopause model parameters r_0, α using a 240-min time window around the zero epoch (onset, peak and end) times. To ensure consistency, we employed a broad time window of 240 minutes to capture the complete pattern in SML, particularly during periods of southward IMF. This time window was uniformly applied to each parameter to maintain
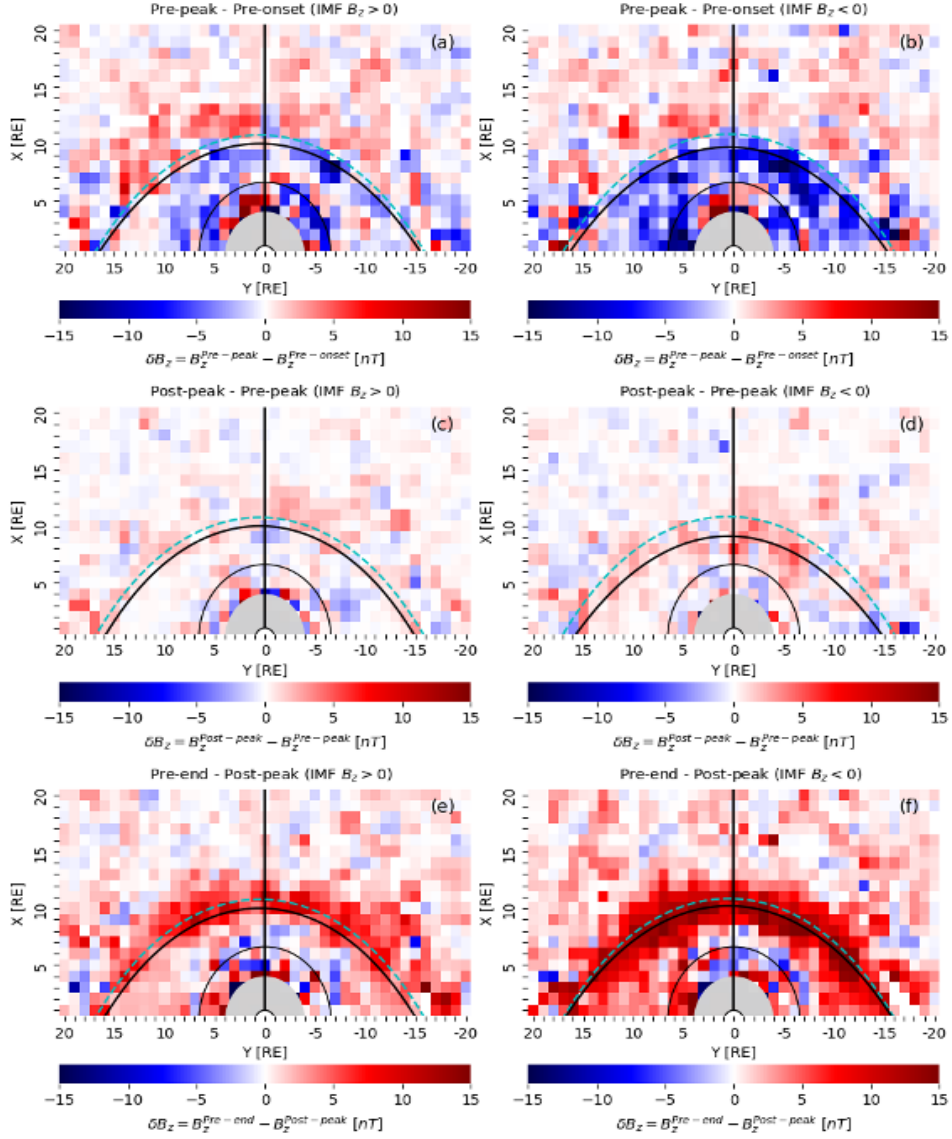
Figure 2. Average differences $\delta B_Z = B_Z^{pre-peak} - B_Z^{pre-onset}$, $\delta B_Z = B_Z^{post-peak} - B_Z^{pre-peak}$, and $\delta B_Z = B_Z^{pre-end} - B_Z^{post-peak}$ indicating changes in magnetic field from substorm onset to peak, around the peak, and from peak to recovery end during northward IMF ($\langle B_Z \rangle > 0$ nT, a, c, e), and during southward IMF ($\langle B_Z \rangle < 0$ nT, b, d, f). The black (cyan, dashed) curves are the same as in the Figure 1 and show the magnetopause location plotted using Shue et al. (1998) model with IMF $B_Z > 5$ (0) nT for northward IMF (left panels) and with IMF $B_Z < -5$ (0) nT for southward IMF (right panels).

195   uniformity throughout the analysis. The blue (red) curves represent the median (mean), the vertical black dotted lines show the zero epoch. The shading indicates the interquartile range between 25% and 75%.
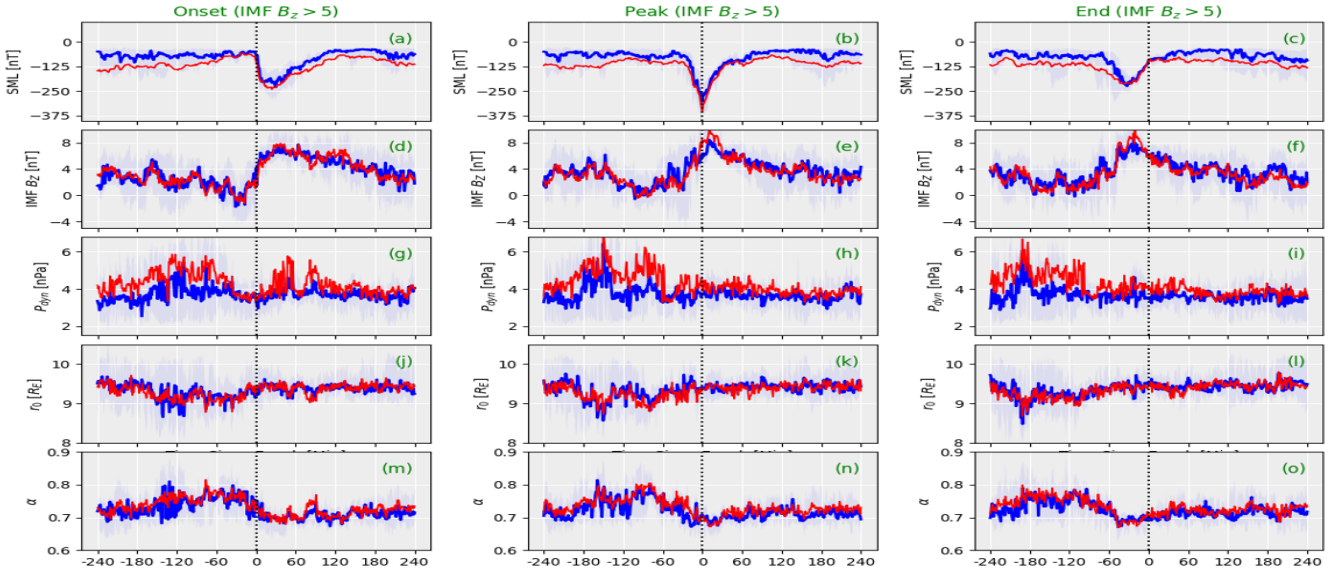
Figure 3. Superposed epoch analysis (median (blue), mean (red), interquartile range (shaded)) of the (*a-c*) SML index, (*d-f*) IMF B_Z, (*g-i*) dynamic pressure P_{dyn}, and magnetopause location parameters (*j-l*) r_0, (*m-o*) α for strongly northward IMF ($\langle B_Z \rangle > 5$ nT). Three zero epoch times are used: (left) substorm onset, (center) substorm peak, and (right) substorm end.

In Figures 3 *a-c*, the SML exhibits a rapid decline or the initiation of a negative bay at substorm onset, reaching its minimum value with a peak magnitude around -250 nT. Subsequently, it ascends towards the pre-onset level (above -100 nT) by the end of the substorm. The duration from substorm onset to peak (expansion phase) is approximately 40 minutes, and from peak to substorm end (recovery phase) is about 70 minutes. As one would expect during northward IMF conditions, this dataset comprises small, relatively short-lived substorms.

Figures 3 *d–f* display that IMF B_Z started to increase a few minutes before the substorm onset, indicating that the substorm onset was associated with a further enhancement of the northward IMF component. The peak of the northward IMF is coincident with the substorm and SML activity peak. The IMF magnitude starts to decrease prior to the end time and continues to do so after the the recovery phase ends.

The solar wind dynamic pressure P_{dyn} results (Figures 3 *g-i*) reveal only very weak changes near the substorm onset time. In the minutes leading to the substorm onset, there is a discernible decrease in the average magnitude of P_{dyn} that reaches its lowest point at the onset. During the substorm peak, the average magnitude of P_{dyn} remains nearly constant and persists at the same level even beyond the recovery phase's end. Figures 3 *j-l* show the magnetopause subsolar location (r_0) evaluated using Equation 2 which gives the standoff distance at subsolar point as function of the upstream solar wind dynamic pressure P_{dyn} and the IMF B_Z. Overall, the changes in the subsolar point location are small during northward IMF. However, the subsolar distance increases toward the end of the growth phase and has a small peak at the substorm onset time. This demonstrates the significant reliance of r_0 on solar wind dynamic pressure, as it exhibits a slight increase during a slight decrease in solar

wind pressure, despite an increase in IMF B_Z near onset. Even after the onset, r_0 follows the trends in solar wind pressure,
continuing beyond the substorm end despite variations in IMF B_Z near the peak and recovery end. Figures 3m-o display
the results for the tail flaring parameter (α, Equation 3). The flaring exponent starts to decrease before the substorm onset,
indicating that there is a reduction in the tail flaring angle at the same time as the subsolar point is moving away from the Earth.
The flaring exponent value is at minimum at the substorm peak, after which it starts to increase slightly again.

Figure 4 displays the results of superposed epoch analysis of SML, IMF B_Z, P_{dyn}, and the magnetopause location param-
eters r_0, α similar to Figure 3 but for strongly southward IMF ($\langle B_Z \rangle < -5$ nT during the interval from substorm onset to the
recovery end. The top row of Figure 4 (a-c) shows clear growth, expansion and recovery phase signatures in the SML index.
The duration of expansion phase is nearly 120 minutes (Figure 4a) for substorms during southward IMF, which is much longer
than the expansion phase for substorms during northward IMF. The substorms are very strong (higher amplitude, $\sim$$-750$ nT)
and their recovery time scale is significantly longer ($\sim$140 min, Figure 4a,b) compared to substorms during northward IMF.
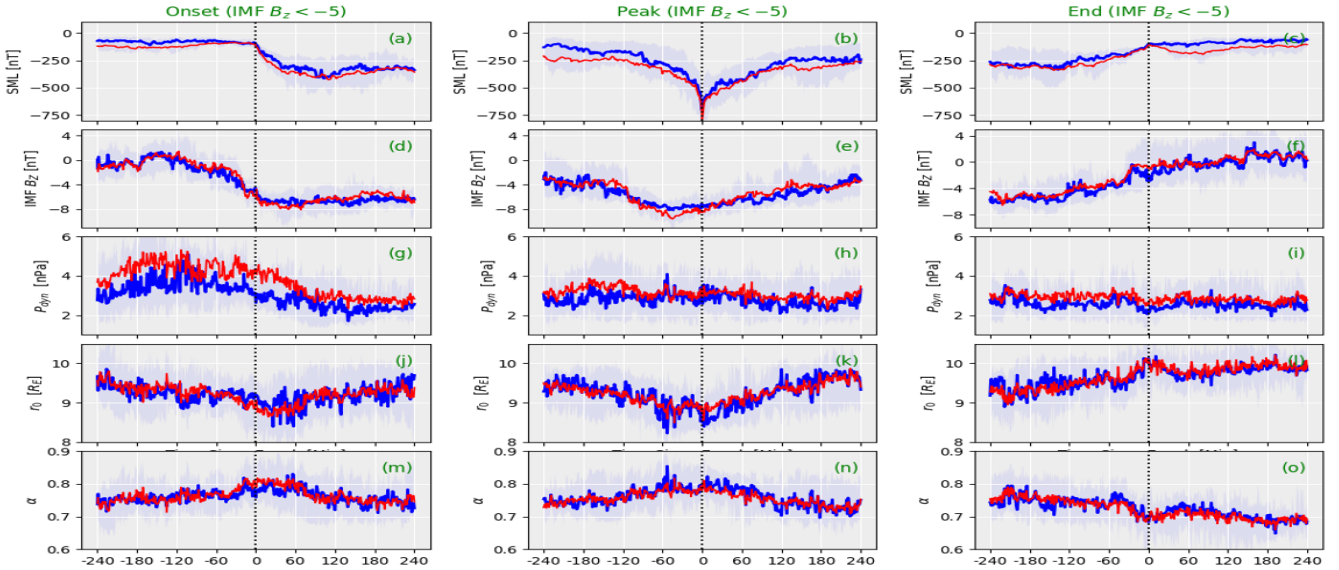
Figure 4. Superposed epoch analysis with the median (depicted in blue), mean (shown in red), and interquartile range (highlighted) of various
parameters: the SML index (a-c), IMF B_Z (d-f), solar wind dynamic pressure P_{dyn} (g-i), magnetopause location parameters r_0 (j-l) and α
(m-o), specifically focusing on instances of strongly southward IMF ($\langle B_Z \rangle < -5$ nT). The analysis is conducted at three distinct zero epoch
times: substorm onset (left), substorm peak (center), and substorm end (right).

Figures 4 d-f show a quite different pattern from the northward IMF case: During the growth phase, IMF B_Z decreases to
reach a minimum at substorm onset, without a signature of northward turning at that time. The IMF B_Z increase starts prior
to the peak time, without a clear timing in relation to the substorm phases, and continues throughout the end of the substorm.
The IMF changes are smooth and broad, indicating that they are not directly associated with the substorm timing.

The dynamic pressure trends (Figures 4 g-i) show a pressure decrease during the growth phase and slightly beyond the onset, while there are no clear trigger signatures either at onset, peak, or end times (note a slight pressure minimum at the substorm end). Figures 4 j-l illustrate the reduction in standoff distance during the substorm growth phase and continuing past the onset. The subsolar distance has a minimum at the peak of the substorm, and starts a gradual increase that continues throughout the recovery phase. The end time is associated with a localized peak in the standoff distance. The inward movement of the magnetopause (decrease in r_0) due to flux erosion during southward IMF (reconnection) is not very pronounced, as the subsolar magnetopause is typically less than 1000 kilometers thick (Paschmann et al., 2018). It is important to note that r_0 strongly depends on the solar wind pressure, as illustrated in Figures 4 (g, j). However, when the pressure is relatively constant (approximately 3 nPa during the Peak and End phases), r_0 is influenced by the trends in IMF B_Z.

Figures 4 m-o show the results for the tail flaring (α). The flaring parameter increases during the growth phase and has a broad peak during the expansion phase (between onset and peak time). The flaring parameter has a minimum at the end of the substorm, coincident with the peak in the standoff distance.

5 Empirical model

The Shue et al. (1998) model is an empirical model developed through a statistical analysis of an extensive dataset of magnetopause crossings, considering the pressure exerted by the incoming solar wind on the magnetosphere and the southward component of the IMF, which plays a pivotal role in the dayside reconnection process at the magnetopause. This model predicts the magnetopause's location as a function of two input parameters (P_{dyn} and IMF B_Z). Based on the predicted location, the model offers an estimation of the magnetopause shape. Due to its simplicity and accuracy under specific solar wind conditions, this model has become a widely utilized tool in space weather research and magnetospheric simulations and therefore, it is employed in this study to estimate the average location of the magnetopause and shape at substorm onset, peak, and end times. The Shue model is solely parameterized by solar wind parameters and was not originally intended to account for substorm variations. However, despite this limitation, its predictions serve as valuable contextual information for interpreting the statistics derived from the magnetopause.

In the panels of Figure 1 and 2, each figure exhibits black and red (cyan) dashed curves are plotted over the average 2D maps of B_Z. These curves are generated using the standoff distance r_0 and flaring angle α parameters from the Shue et al. (1998) model at the times of all 5077 substorm onset, peak, and end times. The values of these parameters at various substorm timings are derived from superposed epoch analysis (see Figures 3 and 4). Utilizing the average values of r_0 and α around substorm key times, we calculate the radial distance r using equation (1) and then determine the positions x_s and r_s through $x_s = r\cos(\theta)$ and $r_s = r\sin(\theta)$. When these x_s versus r_s curves are plotted on the average 2D maps of B_Z for strongly northward or strongly southward IMF ($|B_Z| > 5$), they appear in black in Figure 1 and Figure 2. Additionally, we show northward ($B_Z > 0$) or southward IMF ($B_Z < 0$) model results by red and cyan dashed curves.

In these figures, the Shue magnetopause (red-dashed) passes very closely to the magnetopause, particularly during Pre-onset, signifying the average magnetopause location for northward/southward IMF conditions.During the substorm peak (Post-peak),

the red-dashed curve appears to pass inside the magnetopause for northward IMF (Figure c), indicating a sunward movement of the magnetopause during this phase. In contrast, it passes over the boundary of green color in Figure 1 d and accurately predicts the location of the magnetopause for southward IMF.

265   During substorm end (Pre-end) times, the magnetopause indicates further outward movement for both the northward and southward IMF and this trend is in line with the Shue model. This indicates that during substorms end, the magnetopause is slightly further away from the Earth than predicted by the Shue et al. (1998) model. However, the model curve (black) consistently failed to predict the magnetopause location for both northward and southward IMF ($|B_Z| > 5$) conditions at all substorm timings, as it traverses far within the boundary. The differences between red dashed and black curves are small, but

270   more prominent just before substorm onset (Pre-onset) and after the peak (post-peak) of the substorm during southward IMF Figure 1 b, d.

Substorm phase	Subsolar distance $r_0 [R_E]$			
	$B_Z > 0$	$B_Z > 5$ nT	$B_Z < 0$	$B_Z < -5$ nT
Pr-Onset	10.27	9.30	10.32	9.00
Pre-Peak	10.26	9.65	10.27	8.9
Post-Peak	10.28	9.50	10.33	8.60
Pre-End	10.29	9.70	10.37	9.90

Table 1. Subsolar distances in the Shue et al. (1998) model for the different superposed epoch results. The columns show the values for positive, strongly positive, negative, and strongly negative average IMF B_Z, respectively. The rows indicate times just before substorm onset, before substorm peak, after subtorm peak, and just before substorm end.

The subsolar distances in the Shue et al. (1998) model for various superposed epoch results are presented in four rows in the table, showing their values for positive, strongly positive, negative, and strongly negative average IMF B_Z, respectively. Each row indicates times just before substorm onset, before substorm peak, after substorm peak, and before substorm end.

275   In each case, the magnetopause is shown to be closest to the Earth at the Pre-peak of the substorm (except for $B_Z > 5$), recovering outward from post-peak to the recovery end phase – in line with the in situ measurements (Figure 1 $c - -f$). However, during strong northward, southward IMF, the trend of r_0 deviates from others, showing a closer proximity to the Earth during the Post-peak phase ($B_Z < -5$). Furthermore, comparing the Shue magnetopause location during strongly northward and southward IMF, it is evident that the compression of magnetopause is most pronounced for a strong southward IMF

280   and at the substorm peak (Post-peak). It is important to note that the change in the magnetopause position is very small during substorms from pre-onset to the recovery end. However, the behavior of r_0 is consistent with satellite observation results, as shown in Figure 1. It is well-known that changes in the magnetopause location arise due to variations in the IMF B_Z, dynamic pressure, and other factors. However, its position is heavily influenced by solar wind pressure. We studied separately the variation of r_0 with respect to changes in solar wind dynamic pressure. We found that for pressures ≤ 2 nPa, r_0

285   is approximately 10.7 R_E during pre-onset and 10.73 R_E near the substorm end. For higher pressure (≥ 5 nPa), r_0 is about 8.6

R_E during pre-onset and 8.7 R_E near the substorm end. This indicates that solar wind pressure has a more significant effect on the magnetopause location than the IMF B_Z. However, similar to the results for IMF B_Z changes, the variation in r_0 for solar wind pressure change during substorm phases is minimal and thus not shown in this study.

6 Discussion and Conclusions

290 The magnetopause serves as the boundary layer that demarcates the interface between the solar wind and the magnetospheric plasma. The shape and position of the magnetopause are considerably impacted by two key factors: the dynamic pressure exerted by the solar wind and the strength and orientation of the IMF ((Aubry et al., 1970). Consequently, fluctuations in the solar wind pressure and the presence of a strong northward or southward IMF can induce inward or outward motion of the magnetopause. In this study, we explore variations in the average position of the magnetopause during different phases

295 of magnetospheric substorms. The average location of the magnetopause is determined through magnetic field observations collected by space missions such as THEMIS-A, D, E, RBSP-A, B, and MMS-1 over a five-year period from 2016 to 2020. For the estimation of magnetopose location, we employ the empirical model for magnetospheric shape and size proposed by Shue et al. (1998), incorporating OMNI solar wind data, specifically solar wind dynamic pressure (P_{dyn}) and IMF B_Z, throughout the study period. A list of substorm onsets, identified by a change in the SML index, were obtained from the work of Ohtani

300 and Gjerloev (2020). In order to investigate changes in the magnetopause location during substorm phases, we identified the peak and end times of each substorm in a subset of 5,077 substorms identified within this study period. The initial step involves combining magnetic field measurements from all satellites over the five-year duration and computing the average of the IMF B_Z for each substorm (from onset to recovery end). Subsequently, we filter substorms based on their occurrence during northward IMF ($B_Z > 0$) and southward IMF ($B_Z < 0$). During our observation, we noted that out of 5077 isolated substorms

305 studied in this work, the maximum number of substorms (3458) occurred during periods of southward IMF compared to those during northward IMF (1502). Additionally, there were a few substorms (117) that occurred independent of any IMF changes. We generate average 2D maps of the observed B_Z for northward-southward IMF during distinct substorm phases, including pre-onset, post-peak, and pre-end (Figure 1). The variation in the magnetopause location from substorm growth to recovery phase is clearly visible in that figure. The magnetopause appears to be closest to the Earth during growth phase (pre-onset)

310 for both northward and southward IMF conditions (Figures 1 $a, b,$) and exhibits an outward movement from post peak to the recovery end (Figures 1 $c - f$). However, Figures 1 $c - -f$ illustrate a noticeable outward displacement of the magnetopause, with the movement being less pronounced for the southward IMF compared to the northward IMF.

It is widely acknowledged that substorms have a notable impact on the ring current (Sandhu et al. (2018)), and in turn, the ring current can influence the inward-outward motion of the magnetopause. Therefore, the observed movement of the

315 magnetopause during substorms phases depicted in Figure 1 and Figure 2 could be attributed to the presence and behavior of the ring current. Schield (1969) conducted a survey to evaluate the impact of the ring current on the magnetic field at the boundary of the magnetopause. Their findings indicated that the presence of the ring current could potentially lead to a substantial increase in the subsolar stand-off distance of the magnetopause.

In the difference maps of B_Z shown in Figure 2, an outward movement of the magnetopause from expansion to the recovery phase is confirmed as well, regardless of whether the IMF orientation is northward or southward. This observation aligns with the findings presented in Figure 1.

The magnetopause motion during dayside reconnection could be associated with generation of field-aligned Region 1 and 2 currents (Birkeland, 1908; Iijima and Potemra, 1976).

We used standoff distance r_0 and tail flaring angle α from magnetopause model by Shue et al. (1998). The superposed epoch analysis of solar wind and magnetospheric (r_0, α) parameters for strong northward and southward IMF at substorm phases depicted in Figure 3 and Figure 4, demonstrates a clear relationship of standoff distance with IMF B_Z and solar wind dynamic pressure. Both the figures represent that standoff distance is primarily influenced by the solar wind pressure. However, when the pressure remains relatively constant, the IMF B_Z becomes the driving factor for the standoff distance as illustrated in Figure 3 (d-l) and 4 (d-l). Although, over the years, various other methods have been employed to analyze and approximate the magnetopause location, including empirical models (Dmitriev and Suvorova (2000), Shukhtina and Gordeev (2015), Wang et al. (2013)) and global MHD models (García and Hughes (2007), Lu et al. (2011)). Real-time models like the SWMF (Gombosi et al. (2004), Tóth et al. (2012)) have also been utilized to predict the magnetopause boundary for space weather forecasting analysis.

Figures 3 $d-f$ and 4 $d-f$ reveal a clear correlation between substorm onsets and changes in the IMF direction and indicate substorms occur during strong northward and southward IMF. Which show a consistency with earlier research, which has shown that substorm onsets are associated with intervals of southward IMF (Kokubun, 1972; Wild et al., 2009), as well as with the northward turning of the IMF (Mcpherron et al., 1986; Sergeev et al., 1986; Hsu, 2003).

The average values of the subsolar point r_0 is estimated during substorm onset, peak, and end from Figure 3 ($j-l$) and Figure 4 ($j-l$). To provide a clear representation of these values, they are presented in Table 1 which offers a concise summary of the average subsolar point r_0 at different stages of the substorm.

From the table it is clear that the subsolar point is closest the Earth during substorm growth phase for both IMF $B_Z > 0$, 5 and $B_Z < 0$, -5. It then moves outward from the peak to the substorm recovery end, such that it is farther from the Earth at the end of the substorm than it was at substorm onset form all IMF B_Z. The Shue et al. (1998) predicts the behavior of magnetopause similar to shown in average maps of B_Z (Figure 1). During the substorm phases, it is observed that there is only a minimal change in the subsolar point r_0. However, despite this small change, the behavior of the magnetopause as observed through in-situ measurements and the predictions from the Shue model align with each other. This consistency between the in-situ measurements and the Shue model highlights the robustness of the model in capturing the magnetopause dynamics during substorm events. Despite being solely parameterized by solar wind parameters and not originally intended to account for substorm variations, the Shue model's predictions still provide valuable contextual information for interpreting the statistics derived from the magnetopause, showcasing its usefulness despite this limitation.

In summary, we utilize an extensive dataset from multi-satellite observations and Shue et al. (1998) model to demonstrate the changes in magnetopause position under the influence of northward-southward IMF and internal magnetospheric process

like substorms and we observed that:

(1) The majority of substorms occur during periods of southward IMF, with fewer occurring during northward IMF, and some even happening under stable IMF conditions.

(2) The magnetopause is closest to the Earth during the growth phase of a substorm and shows outward movement during the expansion and recovery phases for $|B_Z| > 0$.

(3) The variation in standoff distance r_0 across the three substorm phases is minimal for both northward and southward IMF conditions.

(4) Shue et al. (1998) model accurately predicts the average magnetopause location during substorm key timings, particularly for northward and southward IMF orientations (IMF $|B_Z| > 0$).

(5) The differences between the substorm-time values and the average conditions indicate that the internal magnetospheric state impacts the location of (and likely processes at) the magnetopause. This may implicate a more complicated relationship between geomagnetic activity and the solar wind driver than illustrated by solar wind - based coupling functions (Newell et al., 2007).

7 Open Research

All data used in this study are available through the NASA Space Physics Data Facility (SPDF, or cdaweb.gsfc.nasa.gov/pub/data, and the SuperMAG website (https://supermag.jhuapl.edu/indices/).

Acknowledgements. We acknowledge the substorm timing list identified by the Newell and Gjerloev technique Ohtani and Gjerloev (2020), the SMU and SML indices Newell and Gjerloev (2011); and the SuperMAG collaboration Gjerloev (2012). This material is based upon work supported by the National Aeronautics and Space Administration under Grant/Contract/Agreement No. 80NSSC21K1675 issued through the Heliophysics Supporting Research Program.

Author contribution. All authors contributed equally to this paper.

Data availability. All data used in this study are available through the NASA Space Physics Data Facility (SPDF, or cdaweb.gsfc.nasa.gov/pub/data, and the SuperMAG website (https://supermag.jhuapl.edu/indices/).
Competing interests. The authors declare that they have no conflict of interest.

References

Akasofu, S. I.: The development of the auroral substorm, Planetary and Space Science, 12, 273–282, https://doi.org/10.1016/0032-0633(64)90151-5, 1964.

Angelopoulos, V.: The THEMIS Mission, Space Science Reviews, 141, 5, https://doi.org/10.1007/s11214-008-9336-1, 2008.

385 Aubry, M. P., Russell, C. T., and Kivelson, M. G.: Inward motion of the magnetopause before a substorm, Journal of Geophysical Research (1896-1977), 75, 7018–7031, https://doi.org/10.1029/JA075i034p07018, _eprint: https://onlinelibrary.wiley.com/doi/pdf/10.1029/JA075i034p07018, 1970.

Auster, H. U., Glassmeier, K. H., Magnes, W., Aydogar, O., Baumjohann, W., Constantinescu, D., Fischer, D., Fornacon, K. H., Georgescu, E., Harvey, P., Hillenmaier, O., Kroth, R., Ludlam, M., Narita, Y., Nakamura, R., Okrafka, K., Plaschke, F., Richter, I.,
390 Schwarzl, H., Stoll, B., Valavanoglou, A., and Wiedemann, M.: The THEMIS Fluxgate Magnetometer, Space Sci Rev., 141, 235–264, https://doi.org/10.1007/s11214-008-9365-9, 2008.

Baker, D. N., Pulkkinen, T. I., Angelopoulos, V., Baumjohann, W., and McPherron, R. L.: The neutral line model of substorms: Past results and present view, Journal of Geophysical Research, 101, 12 975, 1996.

Birkeland, K.: The Norwegian Aurora Polaris Expedition 1902–1903 (Vol. 1), vol. 1, H. Aschelhoug & Co., Christiania, Norway, 1908.

395 Burch, J. L., Moore, T. E., Torbert, R. B., and Giles, B. L.: Magnetospheric Multiscale Overview and Science Objectives, Space Science Reviews, 199, 5–21, https://doi.org/10.1007/s11214-015-0164-9, 2016.

Cahill, L. J. and Winckler, J. R.: Magnetopause crossings observed at 6.6 R_E, Journal of Geophysical Research: Space Physics, 104, 12 229–12 237, https://doi.org/10.1029/1998JA900072, 1999.

Chao, J. K., Wu, D. J., Lin, C. H., Yang, Y. H., Wang, X. Y., Kessel, M., Chen, S. H., and Lepping, R. P.: Models for the size and shape
400 of the earth's magnetopause and bow shock, in: COSPAR Colloquia Series, edited by Lyu, L.-H., vol. 12 of *Space Weather Study Using Multipoint Techniques*, pp. 127–135, Pergamon, https://doi.org/10.1016/S0964-2749(02)80212-8, 2002.

Chapman, S. and Ferraro, V. C. A.: A new theory of magnetic storms, Journal of Geophysical Research, 36, 77, https://doi.org/10.1029/TE036i002p00077, 1931.

Dmitriev, A. V. and Suvorova, A. V.: Three-dimensional artificial neural network model of the dayside magnetopause, Journal of Geophysical
405 Research: Space Physics, 105, 18 909–18 918, https://doi.org/10.1029/2000JA900008, 2000.

Fairfield, D. H.: Average and the unusual locations of the Earth's magnetopause and bow shock, J. Geophys. Res., 76, 6700, 1971.

García, K. S. and Hughes, W. J.: Finding the Lyon-Fedder-Mobarry magnetopause: A statistical perspective, Journal of Geophysical Research: Space Physics, 112, 2006JA012 039, https://doi.org/10.1029/2006JA012039, 2007.

Gjerloev, J. W.: The SuperMAG data processing technique, Journal of Geophysical Research: Space Physics, 117,
410 https://doi.org/10.1029/2012JA017683, _eprint: https://onlinelibrary.wiley.com/doi/pdf/10.1029/2012JA017683, 2012.

Gombosi, T. I., Powell, K. G., De Zeeuw, D. L., Clauer, C. R., Hansen, K. C., Manchester, W. B., Ridley, A. J., Roussev, I. I., Sokolov, I. V., Stout, Q. F., and Tóth, G.: Solution-Adaptive Magnetohydrodynamics for Space Plasmas: Sun-to-Earth Simulations, Computing in Science and Engineering, 06, 14–35, 2004.

Henderson, M. G., Reeves, G. D., Belian, R. D., and Murphree, J. S.: Observations of magnetospheric substorms occurring with no apparent
415 solar wind/IMF trigger, Journal of Geophysical Research: Space Physics, 101, 10 773–10 791, https://doi.org/10.1029/96JA00186, 1996.

Hsu, T.-S.: Occurrence frequencies of IMF triggered and nontriggered substorms, Journal of Geophysical Research, 108, 1307, https://doi.org/10.1029/2002JA009442, 2003.

Iijima, T. and Potemra, T. A.: The amplitude distribution of field-aligned currents at northern high latitudes observed by Triad, J. Geophys. Res., 81, 2165, 1976.

420 Kletzing, C. A., Kurth, W. S., Acuna, M., MacDowall, R. J., Torbert, R. B., Averkamp, T., Bodet, D., Bounds, S. R., Chutter, M., Connerney, J., Crawford, D., Dolan, J. S., Dvorsky, R., Hospodarsky, G. B., Howard, J., Jordanova, V., Johnson, R. A., Kirchner, D. L., Mokrzycki, B., Needell, G., Odom, J., Mark, D., Pfaff, R., Phillips, J. R., Piker, C. W., Remington, S. L., Rowland, D., Santolik, O., Schnurr, R., Sheppard, D., Smith, C. W., Thorne, R. M., and Tyler, J.: The Electric and Magnetic Field Instrument Suite and Integrated Science (EMFISIS) on RBSP, Space Sci. Rev., 179, 127–181, https://doi.org/10.1007/s11214-013-9993-6, 2013.

425 Kokubun, S.: Relationship of interplanetary magnetic field structure with development of substorm and storm main phase, Planetary and Space Science, 20, 1033–1049, https://doi.org/10.1016/0032-0633(72)90214-0, 1972.

Kumar, S., Pulkkinen, T. I., and Gjerloev, J.: Magnetotail Variability During Magnetospheric Substorms, Journal of Geophysical Research: Space Physics, 129, e2023JA031 722, https://doi.org/10.1029/2023JA031722, 2024.

Lin, R. L., Zhang, X. X., Liu, S. Q., Wang, Y. L., and Gong, J. C.: A three-dimensional asymmetric magne-
430 topause model, Journal of Geophysical Research: Space Physics, 115, https://doi.org/10.1029/2009JA014235, _eprint: https://onlinelibrary.wiley.com/doi/pdf/10.1029/2009JA014235, 2010.

Liu, Z., Lu, J. Y., Wang, C., Kabin, K., Zhao, J. S., Wang, M., Han, J. P., Wang, J. Y., and Zhao, M. X.: A three-dimensional high Mach number asymmetric magnetopause model from global MHD simulation, Journal of Geophysical Research: Space Physics, 120, 5645–5666, https://doi.org/10.1002/2014JA020961, 2015.

435 Liu, Z.-Q., Lu, J. Y., Kabin, K., Yang, Y. F., Zhao, M. X., and Cao, X.: Dipole tilt control of the magnetopause for southward IMF from global magnetohydrodynamic simulations: DIPOLE TILT CONTROL OF THE MAGNETOPAUSE, Journal of Geophysical Research: Space Physics, 117, n/a–n/a, https://doi.org/10.1029/2011JA017441, 2012.

Lu, J. Y., Liu, Z.-Q., Kabin, K., Zhao, M. X., Liu, D. D., Zhou, Q., and Xiao, Y.: Three dimensional shape of the magnetopause: Global MHD results: THREE DIMENSIONAL MAGNETOPAUSE, Journal of Geophysical Research: Space Physics, 116, n/a–n/a,
440 https://doi.org/10.1029/2010JA016418, 2011.

Mauk, B. H., Fox, N. J., Kanekal, S. G., Kessel, R. L., Sibeck, D. G., and Ukhorskiy, A.: Science Objectives and Rationale for the Radiation Belt Storm Probes Mission, Space Science Reviews, 179, 3–27, https://doi.org/10.1007/s11214-012-9908-y, 2013.

Mcpherron, R. L., Terasawa, T., and Nishida, A.: Solar wind triggering of substorm expansion onset., Journal of geomagnetism and geoelectricity, 38, 1089–1108, https://doi.org/10.5636/jgg.38.1089, 1986.

445 Newell, P. T. and Gjerloev, J. W.: Evaluation of SuperMAG auroral electrojet indices as indicators of substorms and auroral power, Journal of Geophysical Research: Space Physics, 116, https://doi.org/10.1029/2011JA016779, _eprint: https://onlinelibrary.wiley.com/doi/pdf/10.1029/2011JA016779, 2011.

Newell, P. T., Sotirelis, T., Liou, K., Meng, C. I., and Rich, F. J.: A nearly universal solar wind-magnetosphere coupling function inferred from 10 magnetospheric state variables, Journal of Geophysical Research, 112, 01 206, 2007.

450 Nguyen, G., Aunai, N., Michotte de Welle, B., Jeandet, A., Lavraud, B., and Fontaine, D.: Massive Multi-Mission Statistical Study and Analytical Modeling of the Earth's Magnetopause: 3. An Asymmetric Non Indented Magnetopause Analytical Model, Journal of Geophysical Research: Space Physics, 127, e2021JA030 112, https://doi.org/10.1029/2021JA030112, _eprint: https://onlinelibrary.wiley.com/doi/pdf/10.1029/2021JA030112, 2022.

Ohtani, S. and Gjerloev, J. W.: Is the Substorm Current Wedge an Ensemble of Wedgelets?: Revisit to Midlatitude Positive Bays, Journal of Geophysical Research: Space Physics, 125, e2020JA027 902, https://doi.org/10.1029/2020JA027902, _eprint: https://onlinelibrary.wiley.com/doi/pdf/10.1029/2020JA027902, 2020.

Paschmann, G., Haaland, S. E., Phan, T. D., Sonnerup, B. U. , Burch, J. L., Torbert, R. B., Gershman, D. J., Dorelli, J. C., Giles, B. L., Pollock, C., Saito, Y., Lavraud, B., Russell, C. T., Strangeway, R. J., Baumjohann, W., and Fuselier, S. A.: Large-Scale Survey of the Structure of the Dayside Magnetopause by MMS, Journal of Geophysical Research: Space Physics, 123, 2018–2033, https://doi.org/10.1002/2017JA025121, 2018.

Russell, C. T., Anderson, B. J., Baumjohann, W., Bromund, K. R., Dearborn, D., Fischer, D., Le, G., Leinweber, H. K., Leneman, D., Magnes, W., Means, J. D., Moldwin, M. B., Nakamura, R., Pierce, D., Plaschke, F., Rowe, K. M., Slavin, J. A., Strangeway, R. J., Torbert, R., Hagen, C., Jernej, I., Valavanoglou, A., and Richter, I.: The Magnetospheric Multiscale Magnetometers, Space Science Reviews, 199, 189–256, https://doi.org/10.1007/s11214-014-0057-3, 2016.

Sandhu, J. K., Rae, I. J., Freeman, M. P., Forsyth, C., Gkioulidou, M., Reeves, G. D., Spence, H. E., Jackman, C. M., and Lam, M. M.: Energization of the Ring Current by Substorms, Journal of Geophysical Research: Space Physics, 123, 8131–8148, https://doi.org/10.1029/2018JA025766, 2018.

Schield, M. A.: Pressure balance between solar wind and magnetosphere, Geophys. Res. Lett., 74, 1275, 1969.

Sergeev, V., Dmitrieva, N., and Barkova, E.: Triggering of substorm expansion by the IMF directional discontinuities: Time delay analysis, Planetary and Space Science, 34, 1109–1118, https://doi.org/10.1016/0032-0633(86)90023-1, 1986.

Shue, J., Song, P., Russell, C. T., Chao, J. K., and Yang, Y.: Toward predicting the position of the magnetopause within geosynchronous orbit, Journal of Geophysical Research: Space Physics, 105, 2641–2656, https://doi.org/10.1029/1999JA900467, 2000.

Shue, J.-H., Chao, J. K., Fu, H. C., Russell, C. T., Song, P., Khurana, K. K., and Singer, H. J.: A new functional form to study the solar wind control of the magnetopause size and shape, Journal of Geophysical Research, 102, 9497, 1997.

Shue, J.-H., Song, P., Russell, C. T., Steinberg, J. T., Chao, J. K., Zastenker, G., Vaisberg, O. L., Kokubun, S., Singer, H. J., Detman, T. R., and Kawano, H.: Magnetopause location under extreme solar wind conditions, J. Geophys. Res., 103, 17,691, 1998.

Shukhtina, M. A. and Gordeev, E.: In situ magnetotail magnetic flux calculation, Annales Geophysicae, 33, 769–781, https://doi.org/10.5194/angeo-33-769-2015, 2015.

Sibeck, D., Lopez, R. E., and Roelof, E. C.: Solar wind control of the magnetopause shape, location, and motion, J. Geophys. Res., 96, 5489, 1991.

Tsyganenko, N. A. and Sibeck, D. G.: Concerning flux erosion from the dayside magnetosphere, Journal of Geophysical Research: Space Physics, 99, 13 425–13 436, https://doi.org/10.1029/94JA00719, _eprint: https://onlinelibrary.wiley.com/doi/pdf/10.1029/94JA00719, 1994.

Tóth, G., Holst, B. v. d., Sokolov, I. V., Zeeuw, D. L. D., Gombosi, T. I., Fang, F., Manchester, W. B., Meng, X., Najib, D., Powell, K. G., Stout, Q. F., Glocer, A., Ma, Y.-J., and Opher, M.: Adaptive Numerical Algorithms in Space Weather Modeling, J. Comput. Phys., 231, 870–903, https://doi.org/10.1016/j.jcp.2011.02.006, 2012.

Wang, J., Guo, Z., Ge, Y. S., Du, A., Huang, C., and Qin, P.: The responses of the earth's magnetopause and bow shock to the IMF B_z and the solar wind dynamic pressure: a parametric study using the AMR-CESE-MHD model, Journal of Space Weather and Space Climate, 8, A41, https://doi.org/10.1051/swsc/2018030, 2018.

490 Wang, Y., Sibeck, D. G., Merka, J., Boardsen, S. A., Karimabadi, H., Sipes, T. B., Šafránková, J., Jelínek, K., and Lin, R.: A new three-dimensional magnetopause model with a support vector regression machine and a large database of multiple spacecraft observations, Journal of Geophysical Research: Space Physics, 118, 2173–2184, https://doi.org/10.1002/jgra.50226, 2013.

Wild, J. A., Woodfield, E. E., and Morley, S. K.: On the triggering of auroral substorms by northward turnings of the interplanetary magnetic field, Annales Geophysicae, 27, 3559–3570, https://doi.org/10.5194/angeo-27-3559-2009, 2009.